Research Applications of a Boundary-Layer Wind Profiler

R. R. Rogers,* W. L. Ecklund,+
D. A. Carter,+ K. S. Gage,+
and S. A. Ethier*

Abstract

A small UHF radar wind profiler was operated over a 40-day period during the summer of 1990 at a site on the windward coast of the island of Hawaii. It provided continuous measurements of winds up to the height of the trade-wind inversion, which varied in altitude from about 2 to 4 km during the course of the experiments. The inversion was readily discernible in the data as an elevated layer of high reflectivity, caused by the sharp gradient of refractive index at that level. With a wavelength of 33 cm, the profiler has about the same sensitivity to light rain as to moderately reflective clear air. The data have provided unexpected information on rain development, wave motions on the inversion, sustained vertical air motions at low levels, and interactions between convection and the inversion echo. This paper gives examples of some of the observations, indicating the wide range of applications of boundary-layer profilers.

1. Introduction

Boundary-layer wind profilers are small, low-power, portable, UHF Doppler radars, originally developed at the Aeronomy Laboratory of the National Oceanic and Atmospheric Administration (NOAA) to support a research program in tropical dynamics and climate. They are sufficiently sensitive to enable wind profiling in clear air from altitudes as low as 100 m up to about 3 km—altitudes generally below the operating range of the larger and more powerful VHF wind profilers. Basic considerations in the design of boundary-layer profilers were outlined by Ecklund et al. (1988). Results from initial field tests with a prototype model were given by Ecklund et al. (1990). Several such systems have been used in field projects in the tropical Pacific and elsewhere (Gage et al. 1991; Neff et al. 1991). Most recently, a model has been designed for shipborne use (Wilson et al. 1991). Experience has shown them to operate reliably with only minimal maintenance.

When equipped with a versatile data system such as the one developed at the Aeronomy Laboratory, a boundary-layer profiler has applications beyond wind profiling. Basically, it can measure the complete Doppler spectrum of atmospheric targets with a time resolution on the order of 1 min and a range resolution of about 100 m. In clear air, these data may be used to observe the radial velocity of the wind and its variations in one or more directions and to estimate from the Doppler spread the intensity of small-scale turbulence. This kind of information can be used to estimate eddy dissipation rates (Gage et al. 1980) and is useful in boundary-layer studies (White and Fairall 1991). In rain the Doppler spectrum contains information about both drop motions and air motions, depending on the relative reflectivity of the drops and the clear air. Bimodal spectra in which the clear air and the precipitation modes are clearly distinguishable enable the measurement of drop fall speed relative to the air and hence the drop-size distribution (Wakasugi et al. 1986; Gossard 1988; Currier 1990). These additional applications are all possible without interfering with wind profiling.

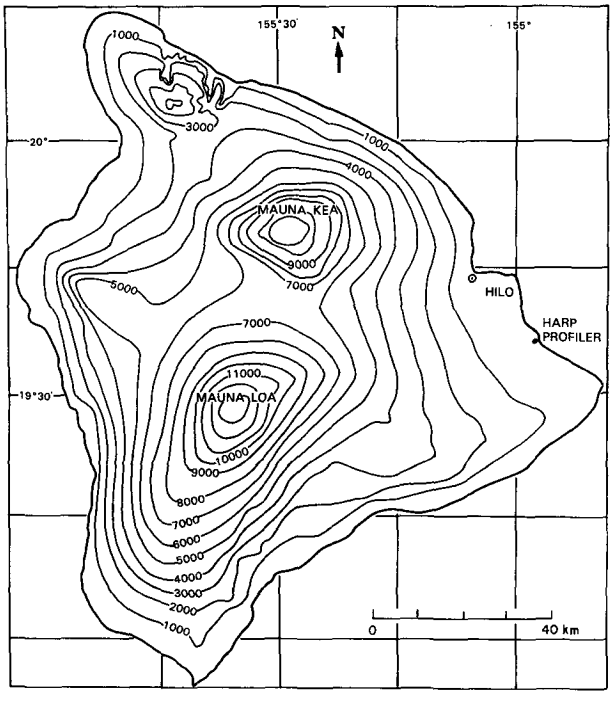

FIG. 1. Topographic map of the island of Hawaii showing location of HARP profiler. Contour interval is 1000 ft.

*Department of Meteorology, McGill University, Montreal, Canada
+Aeronomy Laboratory, NOAA, Boulder, Colorado

As part of the Hawaiian Rainband Project (HARP) during the summer of 1990, a boundary-layer profiler was operated for six weeks at a site 20 km southeast of Hilo, Hawaii (see map, Fig. 1). The data give a unique view of the structure of the dominant trade-wind flow, including the nocturnal katabatic circulation, and have revealed unexpected phenomena such as persistent low-level upward air motions, possibly indicative of standing waves produced by an interaction of the airflow with the island barrier, and gravity waves on the trade-wind inversion. The data have also been used for drop sizing and for studying the development of rain with distance fallen through cloud. In addition, the observations suggest hitherto unreported interactions between rain and clear-air echoes.

This paper gives examples of observations with the HARP profiler, demonstrating the important contributions that a small and inexpensive UHF radar can make to research in atmospheric dynamics and precipitation physics.

2. The HARP profiler

The HARP profiler is one of a series of UHF boundary-layer radars developed at the Aeronomy Laboratory. Table 1 summarizes its characteristics and operating parameters. The antenna consists of four interconnected modules. Each module is a square panel 91 cm on a side and 2 cm thick, composed of 16 individual antenna "patches" connected by microstrip transmission lines. The antenna is mounted on a belt-driven, steerable pedestal designed and built especially for this model by the Surface and Sounding Systems Facility of the National Center for Atmospheric Research (NCAR). Control is accomplished through a PC-based controller/processor developed at the Aeronomy Laboratory and described by Ecklund et al. (1990). As used in Hawaii, the antenna was ordinarily cycled through a sequence of pointing directions that would allow wind profiling and at the same time provide frequent observations in the vertical direction for monitoring the evolution overhead of rainshower structure. This sequence was V–N–V–S–V–E–V–W, where the off-vertical directions were at a zenith angle of 15°. The dwell time at each direction was 30 s and the time for a direction change was 5 s, so that the frequency of vertical observations was close to 1 min^{-1} and the full cycle required just under 5 min.

The data give a unique view of the structure of the dominant trade-wind flow . . . and have revealed unexpected phenomena such as persistent low-level upward air motions . . . and gravity waves on the trade-wind inversion.

Table 1. HARP profiler characteristics.

Frequency	915 MHz
Wavelength	32.8 cm
Peak power	400 W
Pulse duration	0.7 μs
Pulse repetition period	50 μs
Antenna aperture	1.8 m x 1.8 m
Antenna type	Microstrip array
Beamwidth (one-way)	9°
Number of range samples	49
Sample spacing	105 m
Maximum radial velocity	±10.9 m s^{-1}
Number of spectral points	64

Each measurement is a 30-s average during the time the pointing direction is fixed. Substantial integration is needed to detect and measure the generally weak clear-air echoes; 30 s is found to be a reasonable compromise between sensitivity and time resolution. Recorded are the mean Doppler velocity, the Doppler spread, the receiver noise level, the signal-to-noise ratio, and the complete Doppler spectrum at the 49 ranges sampled. The data processor is highly flexible, enabling the display and printout of the data in different formats in real time or in later analysis and the calculation of wind profiles for specified averaging times and consensus windows.

Figure 2a is an example of one of the standard real-time displays, Doppler spectra stacked in altitude (sometimes called the "waterfall" display). This example is for the vertical beam in drizzle conditions. The plotting option employed here is that the spectra are linear in power and normalized so that the maximum spectral amplitude at each level is full scale. Note that the sign convention is that positive velocities in the Doppler spectrum correspond to motion toward the radar.

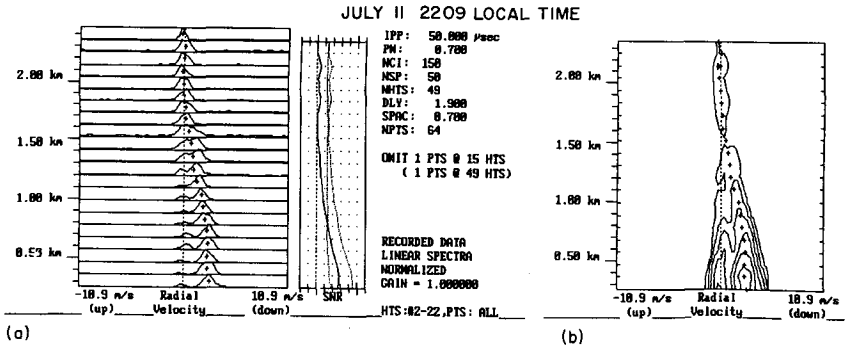

FIG. 2. (a) Doppler spectra measured in the vertical profiler beam in drizzle. Data are plotted for gates 2–22, extending from 255 to 2355 m altitude above ground level. The spectra are linear in power, with the maximum amplitude of each one normalized to full scale. Positive Doppler velocities are *toward* the radar, negative velocities *away from* the radar. The plus sign on each spectrum indicates the mean Doppler velocity, determined by calculating the first moment of the spectrum. The signal-to-noise ratio (SNR) is plotted as a profile on the right. The heavy solid curve is the SNR. The scale (unlabeled) is linear in dB, extending from –20 to 60 dB. The heavy dashed line indicates SNR = 0 dB. (b) The same data as in (a), plotted as spectral envelopes. The outer contour defines the velocities where the spectra are 10 dB above noise; the contour interval is 5 dB. Plus signs indicate mean Doppler velocities, as in Fig. 2a. The echoes above 1.5 km are from the clear air in the trade-wind inversion. Those below are predominantly from small raindrops but also contain a clear-air contribution, as indicated by bimodal spectra.

At the higher altitudes, the spectra are unimodal, centered near a velocity of zero, indicative of scattering by the clear air with negligible vertical air motion. At lower altitudes, the spectra are bimodal, with the higher-velocity mode arising from small raindrops and the lower-velocity mode accounted for by the air. The increase with downward distance of drop fall speed relative to the air is indicative of larger drops at the lower altitudes. To be distinguishable, drops must first provide a detectable cross section, as determined by their sizes and concentration, and, second, fall fast enough relative to the air to be resolved in the spectrum. The resolution of the Doppler spectra for the HARP profiler is 0.34 m s^{-1}. A drop falling this fast relative to the air has a diameter of about 0.12 mm. By convention, the division between cloud droplets and raindrops is drawn at about 0.1 mm. The HARP profiler is therefore just about able to resolve small raindrops (drizzle), but not cloud droplets. Turbulence and wind shear in the sample volume broaden the spectral modes of the drops and the clear air and reduce further the ability to distinguish small drops. Even a uniform wind causes some spectral broadening because of the wide beam of the profiler, but this effect is easy to estimate and is usually less important than the others.

The same data are plotted a different way in Fig. 2b, using another of the real-time display options. These are contours of spectral amplitude on the same velocity–height coordinates as Fig. 2a. The outer contour here is selected to be 10 dB above noise, and the contour interval is 5 dB. The bimodal shape of the spectra is evident in this presentation as two lobes below 1.5 km. This display has a wider dynamic range than Fig. 1a, because the spectral amplitudes are referred to a logarithmic rather than a linear scale.

Figure 3 shows the real-time display of a wind profile. The wind speed and direction are plotted at each of the gate positions where a consensus is found—in this case for a 30-min sampling period. (For an introduction to the data processing and consensus-averaging used in wind profiling, the reader may consult Strauch et al. 1984.) The example in Fig. 3 shows the influence of a downslope (katabatic) wind at altitudes below 1 km and northeasterly trade winds above this level. Maximum speeds are 9 m s^{-1} in the trades and between 5 and 6 m s^{-1} in the downslope wind. The downslope flow is a nightly occurrence on Hawaii, essentially a drainage current caused by radiative cooling of the air near the ground over the high slopes of Mauna Loa and Mauna Kea. At the profiler site, the downslope circulation interacting

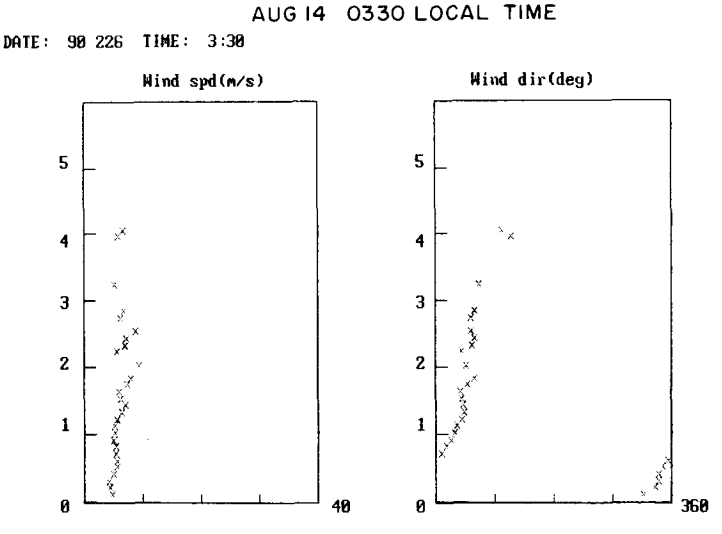

FIG. 3. Vertical profiles of wind speed and direction. The scale of wind speed is linear from 0 to 40 m s^{-1}. The azimuth from which the wind blows is plotted on a scale from 0° to 360°. The vertical scale is in km.

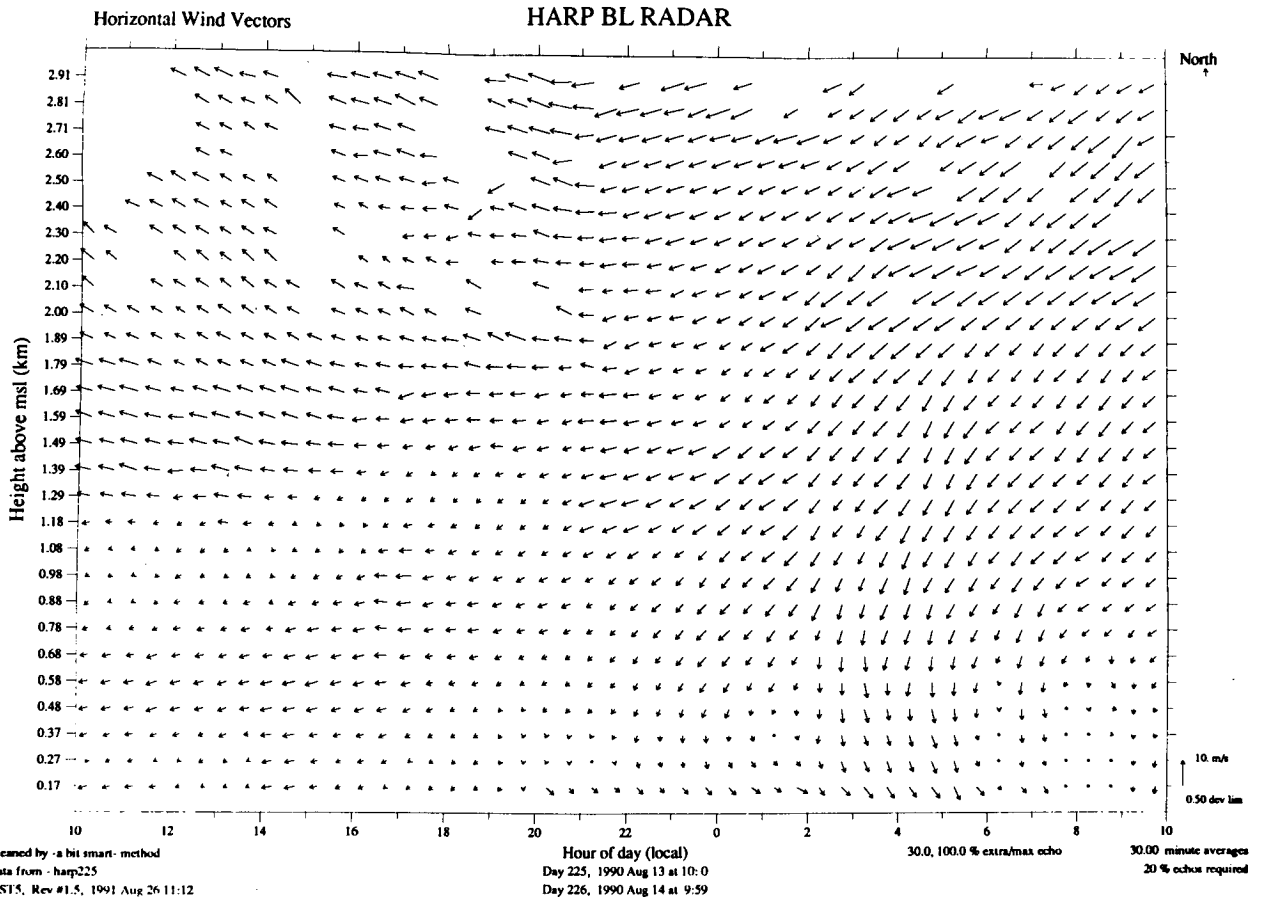

FIG. 4. Time–height pattern of wind vectors for a 24-h period on 13–14 August.

with the trade winds produced a wind from the northwest, as seen here at the lowest altitudes. The profiler data provide the first high-resolution observations of the vertical structure of this circulation over an appreciable time period.

These figures illustrate only three examples of the many displays available in real time. The following sections give examples from further data analysis.

3. Time record of wind profiles

Figure 4 is an example of all the wind profiles measured over a 24-h period (including the one of Fig. 3), plotted as wind vectors. This is the most familiar way of presenting profiler data. Vectors are not plotted at times and ranges for which a consensus was not obtained among the observations in the 30-min averaging period. The clear-air reflectivities were weaker than usual in this example, making some of the data noisy and spoiling the consensus, thus accounting for the gaps in the data at the higher altitudes. This was also a period of uncommonly little rain. Drizzle was briefly overhead at the profiler site at 0830 (all times are LST) on 14 August. Otherwise, there was no evidence of any rain. As a matter of some importance, brief showers or light, widespread rain have little effect on 30-min wind estimates, but longer-lasting, heavy showers introduce time and space irregularities that can cause errors in the wind estimates or interfere with achieving a consensus (Law 1991).

Initially the winds are seen to be weak and generally from the east at altitudes below 1.2 km, and stronger, with a southerly component, above this level. By 2100 on 13 August the wind at the lowest altitude is still weak, but has shifted to the northwest under the influence of the downslope flow. The thickness of the layer affected by this flow increases steadily during the night so that by 0500 the next morning there are north or northwest winds up to a height of 600 m. At higher levels, the winds are from the northeast, the direction of the prevailing trades. A circulation coupling the trade winds and the downslope wind may account for the strengthening of the trades at the time when the downslope flow is most strongly developed.

The pattern in Fig. 4 differs somewhat from the circulation at Hilo, described by Lavoie (1967) and based on hourly surface observations and twice-daily

radiosondes and pibals. Dominating the topography of Hawaii are Mauna Loa and Mauna Kea, each about 4 km high, separated from each other by 40 km on an approximate north–south line, and located inland 40 km from the windward coast. Hilo is at the mouth of the Wailuku River, which drains the broad valley between the two mountains. At night, cool air from the mountains flows down the valley to the east and Hilo. Lavoie notes that with daily regularity the westerly downslope winds reach the Hilo airport at about sunset and persist until three or four hours after sunrise. From pilot-balloon observations at 0700 and 1900, he concluded that the trade winds and the downslope flow form a coupled circulation at least 3 km deep. The circulation is a periodic perturbation on the prevailing trade winds, which in the lowest kilometer produces easterly deviations from the average by day and westerly deviations at night. From 1 to 3 km, the sense of the deviations is reversed: they are westerly by day and easterly at night.

The HARP profiler was located 20 km from Hilo, well south of the Wailuku Valley, on about the flattest part of the island. At this site, the downslope wind was from the north or northwest, not west or southwest as at Hilo, and it arrived later than the time described by Lavoie for Hilo. It is easy to speculate that we were observing not the major component of the drainage flow, as at Hilo, but a weaker branch of the circulation, deflected from westerly to more northerly by interaction with the trades. Even so, the depth of the circulation and its general character appear to be consistent with Lavoie's description.

4. Pattern in the vertical of clear-air reflectivity

The radar reflectivity η of the atmosphere (units m^2 m^{-3}) may be written as the sum of the reflectivity η_a of the clear air and the reflectivity η_d of the drops that constitute rain and cloud. In the UHF range (300 to 3000 MHz) the main mechanism accounting for clear-air reflections is Bragg scattering from spatial irregularities of refractive index created by turbulent mixing in regions in which there is a spatial gradient (usually vertical) of the refractive index. Mixing produces irregularities over a wide range of scales. The radar is sensitive to the spatial scale of half the radar wavelength. Clear air provides a detectable target if the irregularities of this scale are sufficiently strong. For isotropic turbulence in the inertial subrange, the reflectivity of the clear air may be expressed as

$$\eta_a = 0.38\, C_n^2\, \lambda^{-1/3}, \qquad (1)$$

where λ is the radar wavelength and C_n^2 is the structure parameter that characterizes the strength of the refractive index fluctuations (Tatarski 1961).

Rayleigh scattering accounts for the reflections by raindrops and cloud droplets, giving for the reflectivity

$$\eta_d = 0.93\, \pi^5\, Z\, \lambda^{-4}, \qquad (2)$$

where Z is the reflectivity factor of the drops (Battan 1973). Birds and insects also scatter radar waves and may be approximated as Rayleigh scatterers at UHF. Apart from fleeting episodes of interference or occasional odd signals, there is no evidence of birds or insects in the HARP profiler data.

In routine, continuous UHF observations of the lower atmosphere, the reflectivity often either arises entirely from clear air or, when rain is present, is dominated by scattering from drops. In some conditions in light rain, however, the reflectivity of the clear air is comparable to that of the drops. If the type of target is not known, the measured reflectivity may be ascribed entirely to either Bragg or Rayleigh scattering, and expressed accordingly in terms of either C_n^2 or Z. For a given reflectivity, from (1) and (2), these quantities are related by

$$C_n^2 Z^{-1} = 7.49 \times 10^{-16}\, \lambda^{-11/3}, \qquad (3)$$

where C_n^2 is in meters$^{-2/3}$, Z is in millimeters^6 meters^{-3}, and λ is in meters. At the wavelength of the HARP profiler, the relation between the refractive index structure parameter and the rain reflectivity factor that produces the same reflectivity is

$$\log_{10} C_n^2 = \zeta \times 10^{-1} - 13.4, \qquad (4)$$

where $\zeta = 10 \log_{10} Z$ is the reflectivity factor in units of dBZ and C_n^2 is in meters$^{-2/3}$. Thus, a reflectivity factor of 0 dBZ corresponds to a structure parameter of $10^{-13.4} = 4 \times 10^{-14}$; 10 dB$Z$ corresponds to 4×10^{-13}; and so forth. The value of 10^{-11} $m^{-2/3}$, called "very intense" by Gossard (1990), corresponds to a reflectivity factor of 24 dBZ. The sensitivity of the HARP profiler is such that the minimum detectable reflectivity at a range of 2 km corresponds approximately to a reflectivity factor of –20 dBZ and $C_n^2 \approx 4 \times 10^{-16}$.

Figure 5 illustrates a 4-h record of the atmospheric reflectivity and the mean Doppler velocity measured in the vertical beam of the HARP profiler during a mainly fair period on 14 August. The reflectivity is determined from the signal-to-noise ratio through the radar range equation and has been converted here to the refractive index structure parameter C_n^2 using (1). Typical of most fair-weather observations in Hawaii, the highest reflectivities are located in the lowest kilometer and in an elevated layer, here varying in altitude but averag-

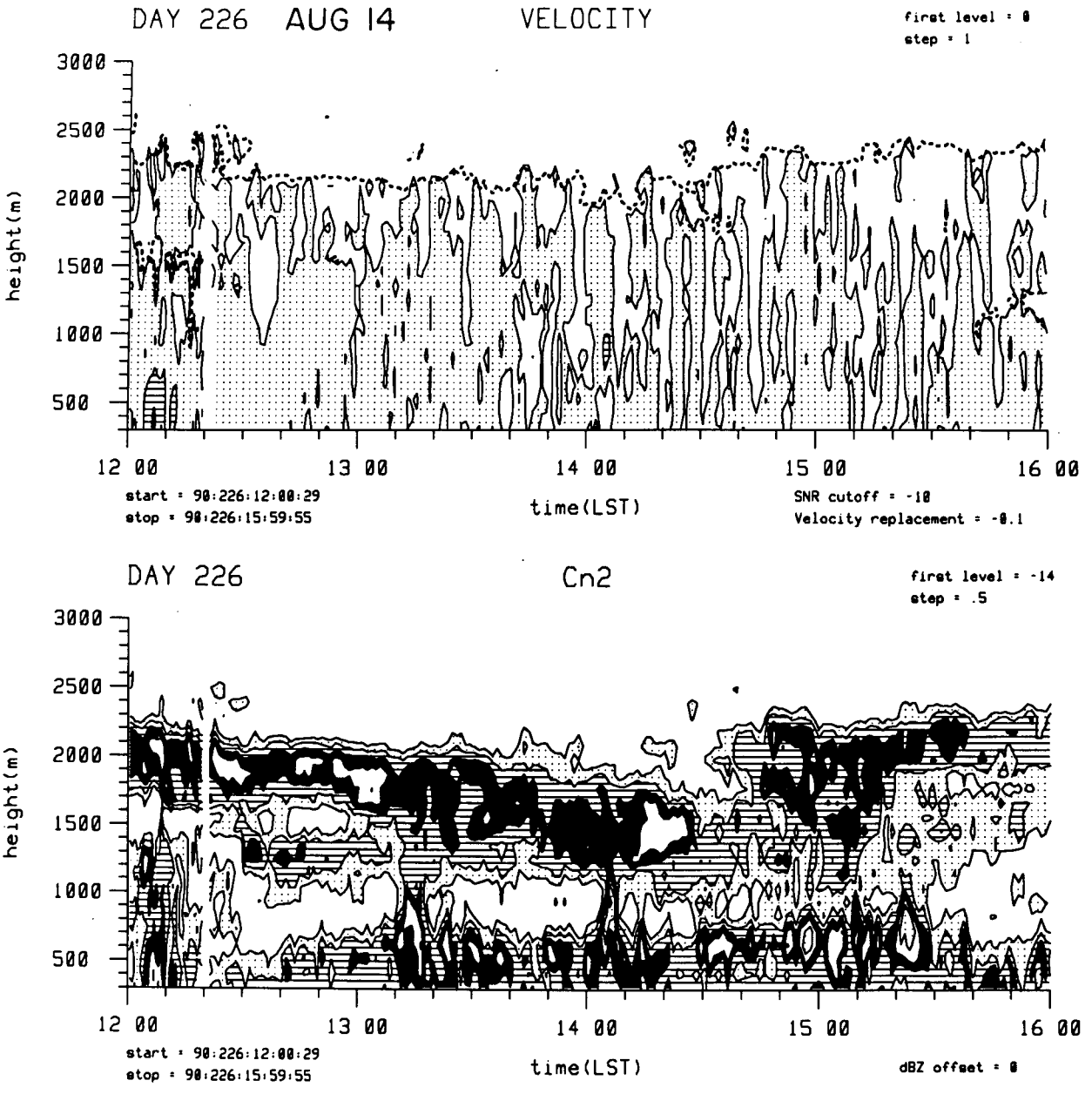

FIG. 5. Time–height pattern of mean Doppler velocity (above) and refractive index structure parameter C_n^2 (below) measured in the vertical profiler beam on 14 August. Four shades (including unshaded) are used in the displays. For C_n^2, the outer contour, which separates clear from the lightest gray shade, is for $C_n^2 = 10^{-14}$ m$^{-2/3}$, or $\log_{10} C_n^2 = -14$. Each successive contour is for an increase of 0.5 in $\log_{10} C_n^2$. To determine the value of C_n^2 at a given point in the pattern, you must count the contours inward to that point. For velocity, any shading indicates downward motion. The contour interval is 1 m s^{-1}. Unshaded regions indicate upward motion. The heavy dashed curve along the top defines the altitude above which the SNR falls below –10 dB. Mean Doppler velocities become unreliable for signals weaker than this value, and are not plotted. A few interior regions also have SNR < –10 dB, and are defined by the dashed lines.

ing about 2 km above the ground. The elevated layer is the trade-wind inversion, visible to the radar because of the strong gradient of refractive index at that level. The refractive index depends on temperature and humidity but the gradient at the inversion is dominated by the sharp decrease of humidity with altitude. The strong echoes at low altitudes are probably also explained by humidity fluctuations, because the surface is a moisture source and gradients are strong near the source. Maximum values of C_n^2 in this example exceed 10^{-12} m$^{-2/3}$ but not 10^{-11}. During the 6-week observing period, the inversion was nearly always detectable as a layer of locally high reflectivity, on some occasions slightly stronger than 10^{-11} m$^{-2/3}$.

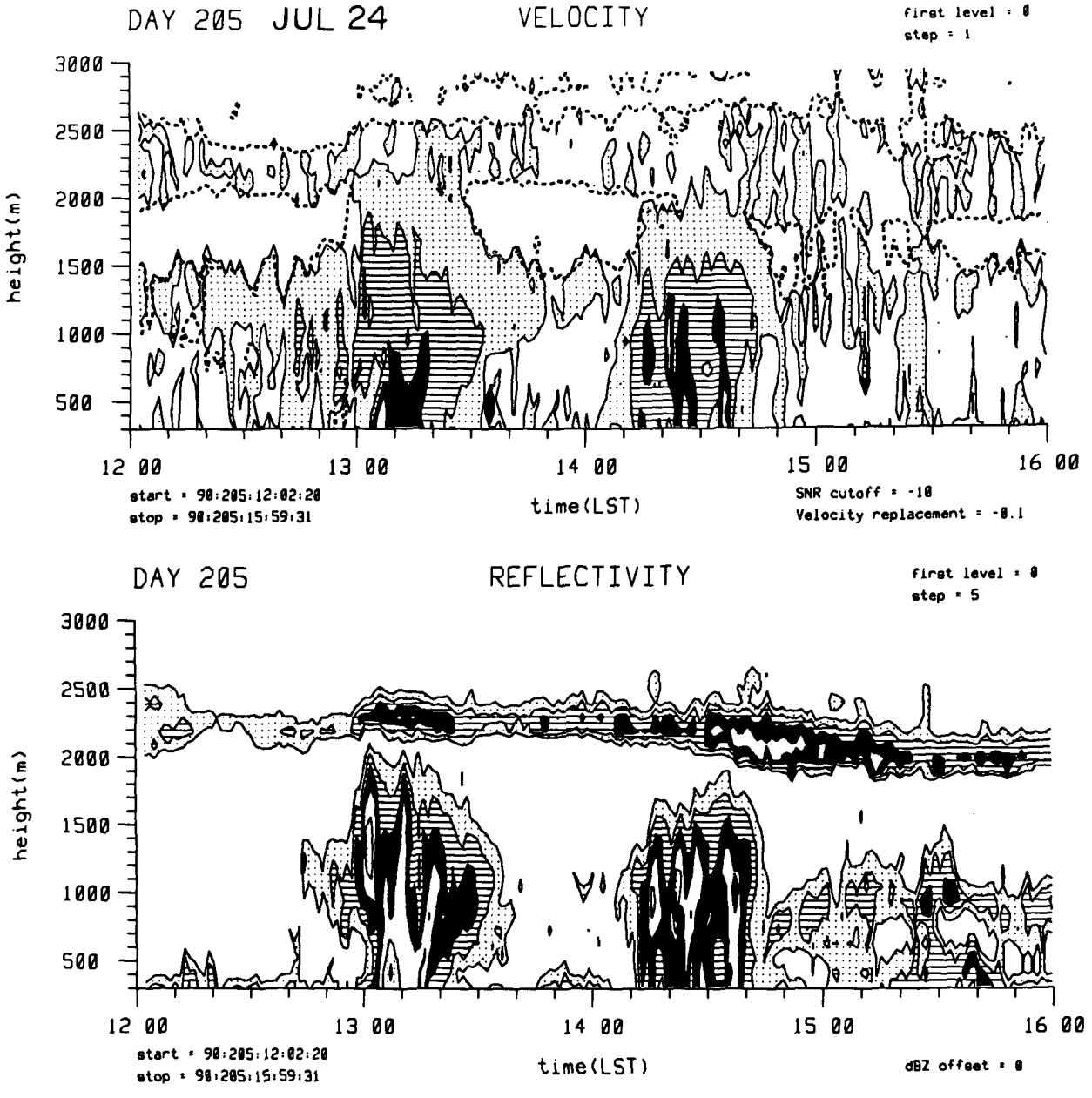

FIG. 6. Time–height pattern of mean Doppler velocity (above) and rain-equivalent reflectivity factor (below) on 24 July. Plotting convention for velocity as in Fig. 5. For reflectivity factor, the outer contour is 0 dBZ and the contour interval is 5 dBZ.

Its height varied from a little below 2 km to about 4 km. The altitude in this example is lower than average.

The upper part of Fig. 5 shows the pattern of mean Doppler velocity in the vertical beam. Any shading indicates downward motion; unshaded regions indicate upward motion. The small region of downward velocities greater than 1 m s^{-1}, located below 500 m at 1208, is probably caused by drizzle. No other rain is present, though some of the data at midlevels may be influenced by clouds. Alternating upward and downward motions at a given level suggest atmospheric waves or oscillations. The vertical extent of some of these oscillations is a kilometer or more.

5. Mixed rain and clear-air echoes

Figure 6 is another example of a 4-h record of reflectivity and mean Doppler velocity in the vertical profiler beam. Two rainshowers are included in the record. The reflectivity here has been converted to the rain-equivalent reflectivity factor using (2). The outer

contour of 0 dBZ in this plot is considerably above the minimum detectable signal, but is helpful in distinguishing the predominantly rain echoes below from the inversion layer above. Also, this threshold for the outer contour is about 6 dB higher than that used in Fig. 5; some of the weaker echoes in that figure would not appear here because of the higher threshold. The maximum reflectivity factors in the showers are about 25 dBZ. In the inversion echo, the maxima slightly exceed 15 dBZ, and are equivalent to C_n^2 values of about 10^{-12} m$^{-2/3}$. The maximum downward velocities in the showers are close to 4 m s^{-1}, the fall speed of a drop 1 mm in diameter.

This example is fairly typical of much of the data, in that it contains a mixture of rain and clear-air echoes. As defined by the 0-dBZ contour, the showers are distinct from the inversion. This is not always so, for in some instances showers penetrate the inversion and extend several hundred meters above it. Moreover, some echoes are not readily identifiable from profiler data alone as rain or clear air. In this example the echoes extending upwards to about 1.5 km between 1500 and 1600 LST are at the level of the previous showers but are probably predominantly clear air, because the velocity pattern shows no downward velocities large enough to indicate drops. The complete spectral data, such as the example of Fig. 2, are a more sensitive indicator of small drops than the mean Doppler velocity alone. As another example of possible ambiguity, it is obvious in Fig. 6 that the inversion echo is stronger at the times of the showers or just following them. This is observed frequently but not invariably in the profiler records. A possible explanation is that through vertical mixing the showers inject some cloud material into the inversion layer, which causes a temporary and local strengthening of the echo. A preliminary examination of spectral data in these situations has not revealed the presence of drops, but this does not prove their absence since they would not be detectable if small enough. Another possibility is that the upward motion of moist air associated with the shower causes a sharpening of the vertical gradient of the refractive index in the inversion, leading to a stronger reflectivity. Explanation of this observation may have to await the analysis of aircraft data on the composition of the inversion layer.

6. Wave motions on the inversion

The variations of the vertical velocity at the inversion level in Figs. 5 and 6 appear unorganized and might be explained by either intermittent gravity waves or the passage overhead of convective plumes or thermals. Figure 7 is an example that provides clear evidence of waves. As in Fig. 6, the reflectivity pattern shows a mix of rain and clear-air echoes. The inversion echo is well defined by the 0-dBZ contour ($C_n^2 = 4 \times 10^{-14}$). Four showers about 45 min apart are indicated by the regions of downward velocities exceeding 2 m s^{-1}. The maximum clear-air reflectivities at low altitudes are located not at the lowest levels in this example but at heights of 600 to 800 m. This lifting of the level of maximum reflectivity is often observed between midnight and 0900 local time and is tentatively ascribed to the downslope wind. For reasons as yet unknown, the air in the downslope flow is evidently less reflective than the air from over the water. When the downslope circulation is established, the more reflective air is replaced near the ground by the cooler downslope air, and the reflectivity at those levels is reduced.

Most remarkable . . . is the apparent regularity of the oscillations in the inversion.

Most remarkable in Fig. 7 is the apparent regularity of the oscillations in the inversion. This impression was confirmed by spectral analysis of the data. The spectrum of the velocity fluctuations in the inversion in Fig. 7 (not shown) reveals a predominant component with a period of about 6 min and a significant secondary component with a period of 18 min. Spectra of the data in Figs. 5 and 6 are quite different. They are relatively flat but do have significant content at periods from 8 to 20 min. About all we can conclude from this preliminary analysis is that there are significant differences in the velocity fluctuations in the cases considered, although each example has spectral components within the frequency range expected for gravity waves. Much work remains to determine how the intensity of the velocity fluctuations and the spectral shape depend on environmental conditions.

7. The inversion echo and convective clouds

Figure 8 is a sequence of spectral data obtained with the vertical beam during a 10-min period when cumulus clouds were passing overhead. Initially, at 1747:26, the inversion appears as a weak local maximum at an altitude of 2.3 km. Echoes extend from there to the ground with additional local reflectivity maxima at 2 and 0.7 km. Mean vertical velocities are near zero at all levels. The next three frames show a blooming and lifting of the inversion echo and a

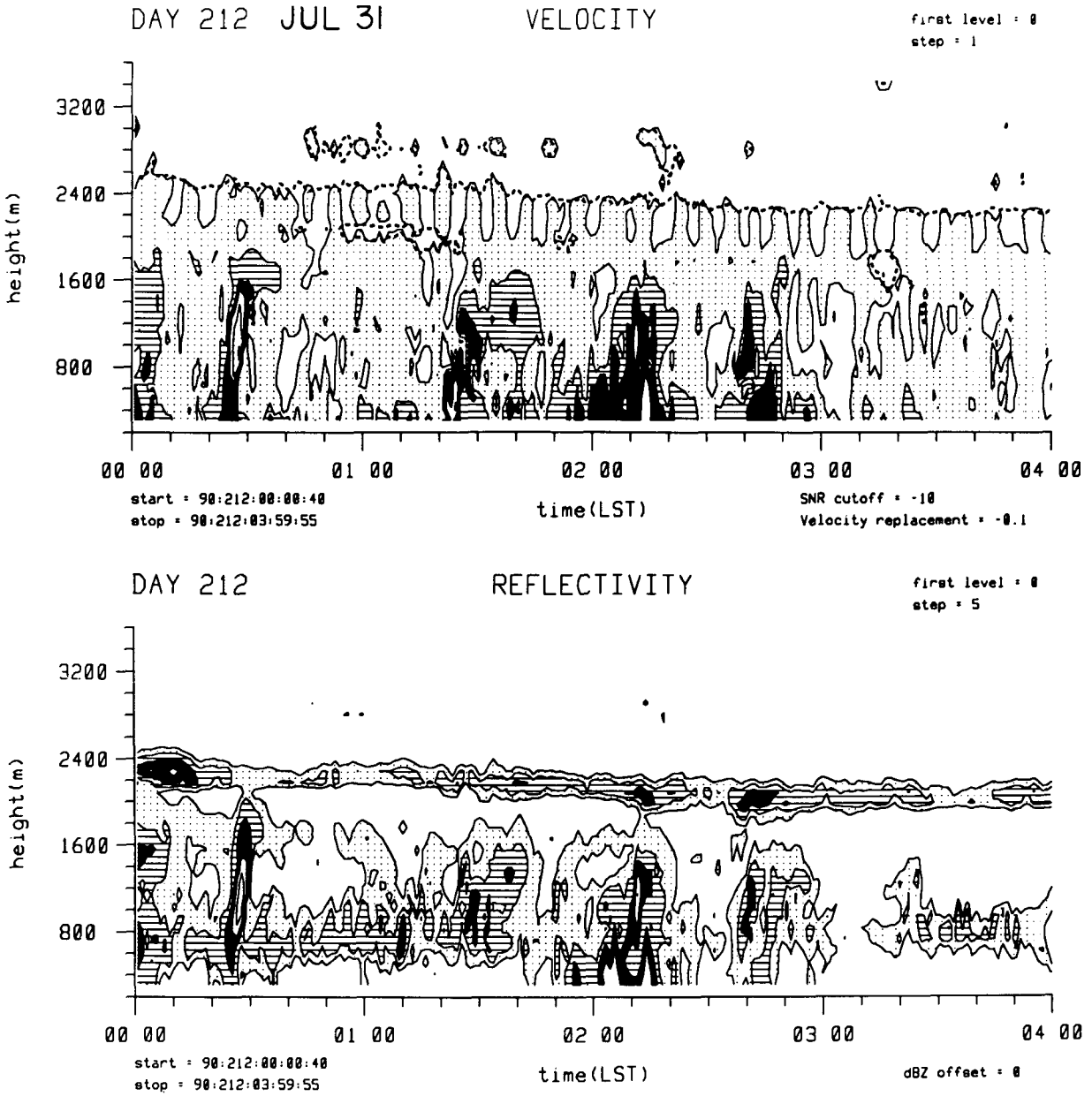

FIG. 7. Patterns of velocity and reflectivity factor on 31 July. Plotting conventions as in Fig. 6.

billowing of the pattern below the inversion. At 1749:47 the inversion is several hundred meters higher than it was initially, its reflectivity has increased by 15 dB, and the standard deviation of the Doppler spectrum (measured but not plotted) has increased from 0.6 initially to 3.4 m s^{-1}. The spectrum is equally broad at 2 km, and centered on an upward velocity of 5.7 m s^{-1}. These dramatic changes in a period of only 2 min occurred as a cumulus cloud drifted into the beam. The cloud obviously contained a vigorous and turbulent updraft, which reached and slightly penetrated the inversion level. The strengthening of the signal at that level is probably accounted for partly by the injection of cloud droplets and partly by an intensification of the clear-air echo. The increase in mechanical turbulence could explain a strengthening of the clear-air echo, as could any sharpening of the gradient of refractive index by the convective cloud pushing up from below.

The effects of the cloud subside until 1755:05, when the updraft at 2 km strengthens and the spectrum there broadens. In nearly every frame, downward motion is indicated at the inversion; that motion is now at its strongest, with a mean downward velocity of 3.0 m s^{-1} at 2.3 km. It is not clear whether the downward motions at the inversion are indicative of an adjustment following the overshooting of negatively buoyant

air, or whether they are part of a gravity wave at that level. The only evidence of any rain in these patterns is a weak suggestion of drizzle at about 1.5 km altitude by the slight bulge of the contours toward positive velocities at 1753:54 and in the last two frames. The data presented here thus represent a vigorous convective cloud that contains little rain. On the other hand, rainshowers often occurred in benign conditions, without strong turbulence or vertical air motions. Their interaction with the inversion may be less significant than that of vigorous but nonprecipitating clouds like the one in Fig. 8.

8. Persistent low-level updrafts

A fairly common observation, especially at night, was sustained upward air motions at altitudes up to about 1 km for periods of an hour or longer. Often exceeding 1 m s^{-1}, these vertical velocities are too strong to be explained simply by orographic lifting of the trade winds. The terrain at the profiler site was tilted downward toward the northeast, but with a slope of only about 1/60. Orographic lifting of a strong trade wind of 10 m s^{-1} would thus account for a vertical velocity of only a few tenths of a meter per second. Figure 9 is an example of a sustained updraft much stronger than explainable by simple orographic lifting.

The velocity pattern shows upward velocities reaching to 1 km or higher during much of the 2.5-h period plotted. Even during the 40-min period around 0100 LST, when several showers passed overhead, the low-level updraft persisted. This is shown more clearly in Fig. 10 in a series of representative spectra over the period plotted. Each example indicates upward air motion at low altitudes. Even at 0110:46, during the time of the showers, upward air motion is evident, though the mean Doppler velocity at the lowest levels is downward, dominated by the raindrop mode of the spectrum. The example at 0148:25 is at the time of the maximum low-level vertical velocity, 3 m s^{-1}. The bimodal tendency of several of the spectra then suggests the presence of small drops. The downward velocities above 1 km appear to be real air motions, however, not just the downward motion of drops. The data give the strong impression that the upward motion at low levels is somehow coupled or related to the downward motion at high levels. Airplane flights over the windward coast of Hawaii sometimes detect regions of strong and persistent vertical air motions, possibly explained as standing waves (W. A. Cooper 1990, personal communication). Also, recent numeri-

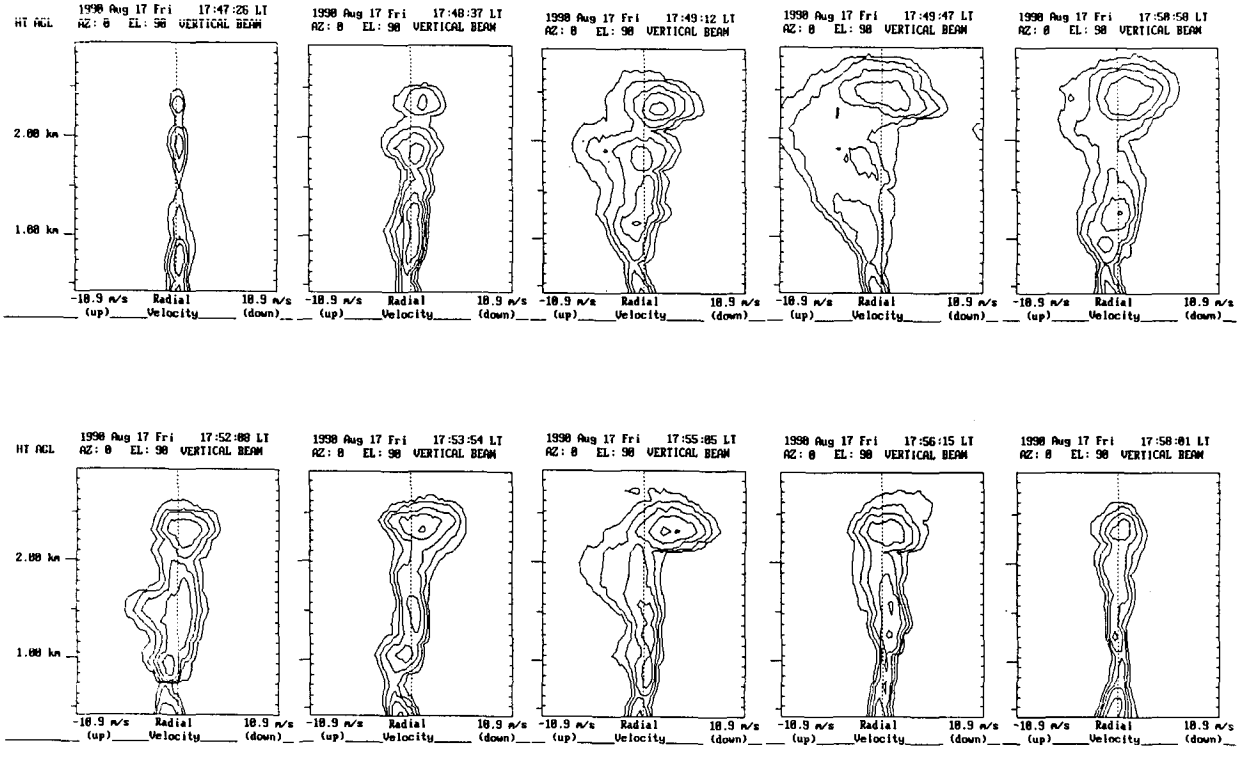

FIG. 8. Sequence of spectral envelopes showing interaction of convective clouds with inversion. Outer contour is 5 dB above noise; contour interval 5 dB.

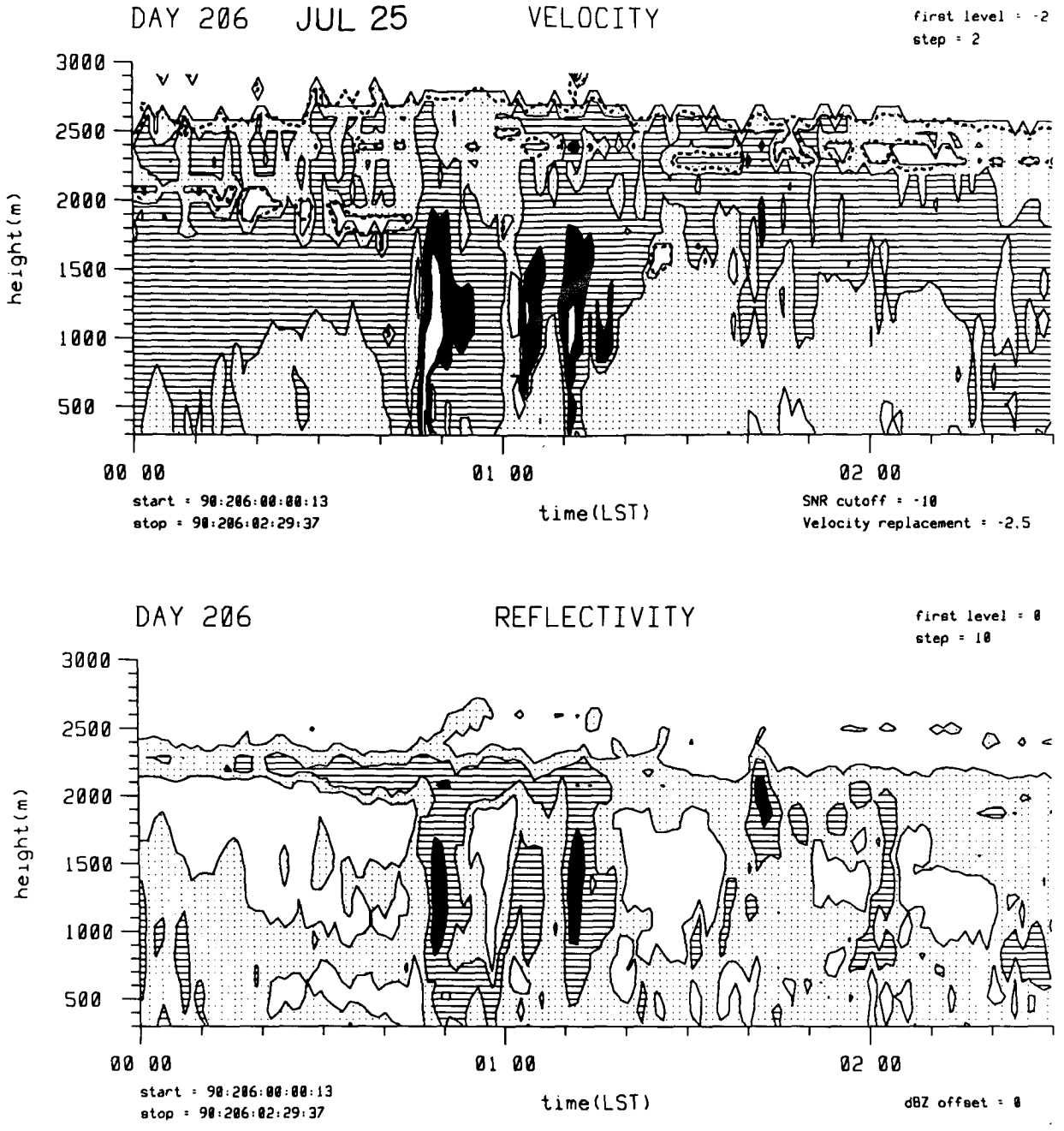

FIG. 9. Patterns of velocity and reflectivity factor during the time of a sustained low-level updraft. For reflectivity, outer contour is 0 dBZ and contour interval is 10 dBZ. For velocity, outer contour is -2 m s^{-1} (an updraft of 2 m s^{-1}) and contour interval is 2 m s^{-1}. Thus, the unshaded areas below 500 m from 0140 local time onward correspond to upward velocities greater than 2 m s^{-1}, and the lightly shaded region extending at times to above 1 km indicates upward velocities from 0 to 2 m s^{-1}. Darker shades are downward velocities.

cal modeling of the airflow over eastern Hawaii sometimes indicates wave motions associated with the downslope flow (Rasmussen and Smolarkiewicz 1993). Our observations appear to be consistent with the existence of such waves, tilted in altitude. A definitive interpretation of the data must await further analysis and comparison with aircraft measurements.

9. Drop-size distributions and rain development

The drop-size distribution of rain is fundamental in the theory of rain development and figures importantly in the remote sensing of rain and in assessing the effects of rain on radio propagation. Attempts to mea-

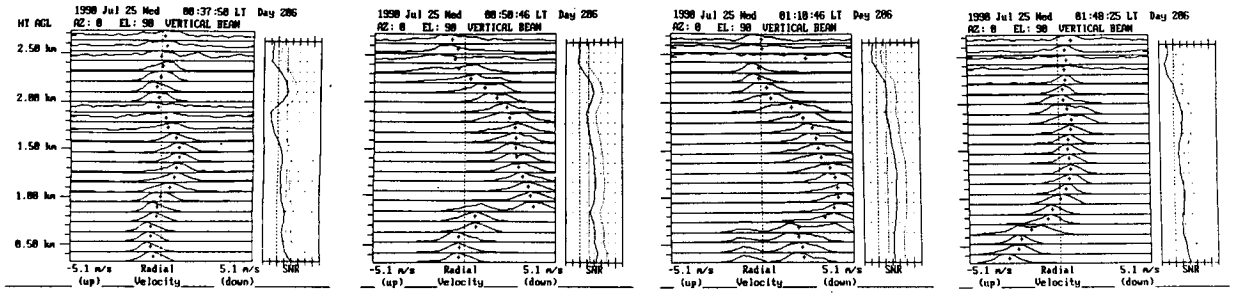

FIG. 10. Spectra at selected times, showing details of the low-level updraft of Fig. 9.

sure the drop-size distribution by Doppler radar go back a long time (Boyenval 1960; Probert-Jones 1960; Rogers and Pilie 1962). Drop size is a known function of the fall speed of a drop relative to air. Measurable by a vertically pointing Doppler radar is the fall speed of drops relative to the radar, which depends on the fall speed relative to the air and the vertical air velocity. The classical problem in radar drop sizing is that the drop-size distribution computed from a given Doppler spectrum is sensitive to the vertical air velocity, which is unknown. Profilers have solved the problem because they are sensitive to the clear air as well as rain. Bimodal spectra such as some of those in Fig. 2, in which the separate modes arising from the drops and the clear air are identifiable, enable the measurement of drop fall speed relative to the air and, hence, the drop-size distribution. This advantage of profilers over ordinary meteorological radars for certain precipitation studies was recognized by Gage and Balsley (1978) and has recently been exploited by Wakasugi et al. (1986, 1987) and Gossard (1988). The technique was thoroughly investigated in the Ph.D. thesis of Currier (1990), and was central to a study of precipitation development by Gossard et al. (1990). Because the HARP profiler has about the same sensitivity to moderately reflective clear air ($C_n^2 \approx 10^{-13}$ m$^{-2/3}$) as to drizzle ($\zeta \approx 5$ dBZ), it is especially well suited for studies of rain initiation and of the light rain that occurs very frequently in Hawaii.

The Doppler spectrum measured by a profiler may be written as

$$S(v) = \eta_a s_a(v) + \eta_d s_d(v) \qquad (5),$$

where $s_a(v)$ is the Doppler spectrum of the air, $s_d(v)$ is the Doppler spectrum of the drops, and η_a and η_d are the reflectivities of the air and the drops, given by (1) and (2). The convention in (5) is that s_a and s_d are normalized to unit area, so that the integral of $S(v)dv$ equals the total target reflectivity. Spectra suitable for drop sizing are those in which the air components $\eta_a s_a$ and the drop components $\eta_d s_d$ are distinguishable and may be separately estimated. (Different approximations have been used to separate the drop spectrum from the air spectrum in the region where they overlap.)

The mean velocity toward the radar of the air in the sampled volume is given by the mean velocity in $s_a(v)$. This velocity is used to convert the Doppler velocity spectrum of the drops to their spectrum in terms of terminal fall velocity. For vertical viewing, the Doppler velocity of a drop is related to its terminal fall velocity, V_t, by $v = V_t - U$, where U is the updraft velocity. Referred to a scale of terminal velocity, the Doppler spectrum of the drops is denoted by $s_d'(V_t)$, and is just the spectrum $s_d(v)$ shifted to the right by the velocity U. That is,

$$s_d'(V_t) = s_d(V_t - U). \qquad (6)$$

The shifted spectrum may be converted to the drop-size distribution by assuming Rayleigh scattering and using an appropriate relationship between drop diameter and terminal fall velocity. Denoted by $N(D)$, the drop-size distribution is then given by

$$N(D) = \beta Z D^{-6} (dV_t/dD) s_d[V_t(D - U], \qquad (7)$$

where Z is the reflectivity factor, D the drop diameter, U the updraft speed, and V_t the terminal velocity of a drop of diameter D. The factor β is the fraction of total reflectivity accounted for by the drops, given by $\eta_d/(\eta_d + \eta_a)$ and estimated from the relative contents of the two spectral modes. In applying this equation, Z is determined from the measured signal strength through the radar equation, U is determined from the mean velocity in the clear-air spectral mode, and $V_t(D)$ is an analytical approximation to the drop fall speeds at standard sea level conditions given by Gunn and Kinzer (1949).

Figure 11 shows the drop-size distributions at altitudes from 1.4 km down to 0.5 km, calculated from the Doppler spectra in Fig. 2. Entered on each of the plots is the following information: altitude, reflectivity factor, and updraft velocity. The reflectivity increases steadily with downward distance from 0.86 dBZ at 1397 m to 13.23 dBZ at 461 m. Weak updrafts are present at altitudes of 1189 and 461 m; downdrafts are present

elsewhere. The dashed lines are the distributions computed from the measured Doppler spectra. A source of error in these distributions is the spreading and smoothing of the Doppler spectrum caused by turbulence, wind shear, and the cross-beam wind component. Each of these effects can cause the Doppler velocity of a drop to deviate from its terminal velocity. The Doppler spectrum is smeared or spread out by these effects in a process that amounts to a convolution of the spectrum of terminal velocity with the spectrum of the air motions. As a refinement in the analysis, the unwanted spreading can be partly removed by deconvolving the Doppler spectrum of the drops by the spectrum of the air. In principle, this sharpens the drop spectrum and compensates for the spurious Doppler broadening, but in practice deconvolution is a noisy process that should only be undertaken with caution. The solid lines are the distributions computed from spectra that have been deconvolved to compensate for spreading by a Gaussian function with a standard deviation of 0.2 m s^{-1}—a function similar to but narrower than the actual air spectrum. This kind of "mild" deconvolution has the effect of compensating for some of the spurious broadening without introducing excessive noise. In these examples the original spectra are relatively smooth and the deconvolution has little effect. The systematic changes of drop-size distribution and reflectivity with distance fallen suggest a gravity-dominated precipitation process in which the raindrops are growing as they fall by sweeping out cloud droplets. Data of this kind have already been used in an assessment of a steady-state sweepout model (Rogers et al. 1991). Work is under way on comparing the observations with predictions of numerical cloud models.

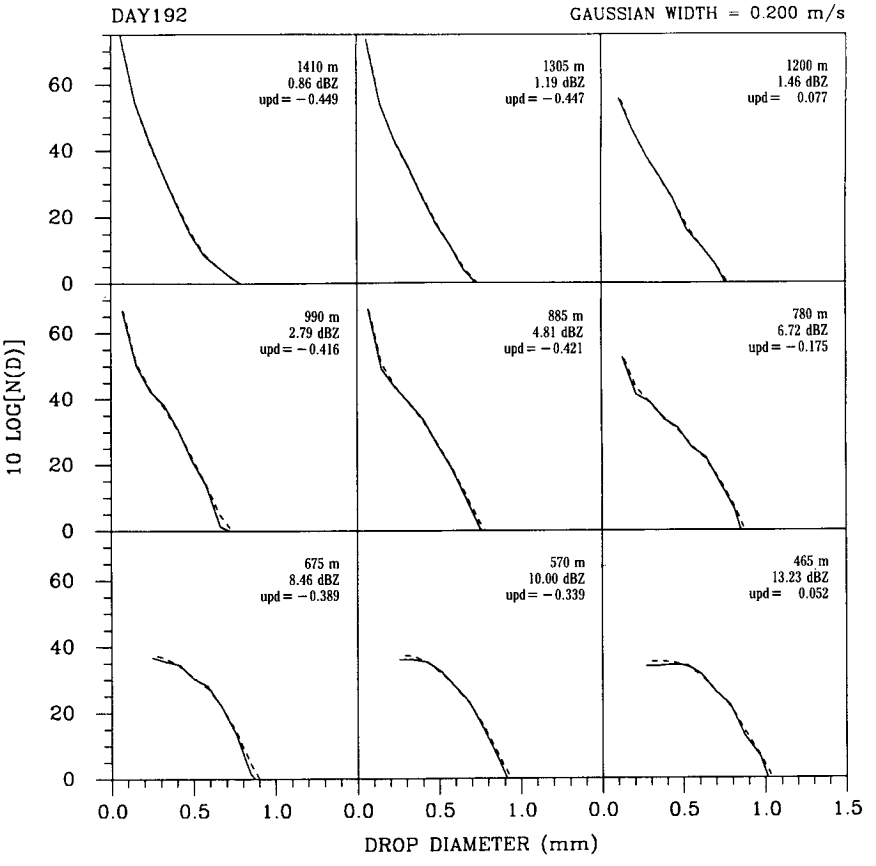

FIG. 11. Drop-size distributions from Doppler spectra in Fig. 2. Dashed lines are distributions from the spectra as measured; solid lines are from the spectra deconvolved to compensate for undesirable spectral spreading, as explained in the text.

10. Conclusions

Experience with a boundary-layer profiler in HARP has provided many examples of the contributions this new kind of radar can make to research. Because it is equally sensitive to light rain and clear air, the profiler can be used for investigations of precipitation structure and development in addition to wind profiling. The windward side of Hawaii was an especially favorable setting for these exploratory measurements because of the high frequency of occurrence of rain and the persistence of strong clear-air echoes associated with the trade-wind inversion. Routine measurements of both the wind profile and the reflectivity and vertical velocity of showers were feasible. Under appropriate conditions, drop-size distributions could also be estimated, based on the complete Doppler spectrum. In addition to fulfilling these established measurement techniques, the profiler revealed unexpected phenomena such as gravity waves on the inversion, persistent vertical motions at low altitudes, and complex interactions between cloud and clear-air echoes—all exciting topics for future research.

Acknowledgments. The idea of taking a profiler to Hawaii on the HARP project originated with R. A. Kropfli of the NOAA Wave

Propagation Laboratory. Plans were set in motion when one of us (RRR) was a visitor at WPL and the National Center for Atmospheric Research. We are grateful to Bob Kropfli and W. A. Cooper for making the visit possible and for their early encouragement. E. E. Gossard of CIRES contributed substantially to the planning of the project and is thanked for the many days he spent teaching us about the application of profilers to precipitation measurement. We thank Margaret LeMone of NCAR, who reviewed the manuscript for the *Bulletin* editors, for many helpful suggestions. This research was sponsored by the Office of Naval Research, the Atmospheric Environment Service of Canada, and the National Science Foundation under Agreement ATM-8720797.

References

Battan, L. J., 1973: *Radar Observation of the Atmosphere.* University of Chicago Press, 324 pp.

Boyenval, E. H., 1960: Echoes from precipitation using pulsed Doppler radar. *Proc. 8th Weather Radar Conf.,* San Francisco, Amer. Meteor. Soc., 57–64.

Currier, P. E., 1990: Precipitation measurement using a dual frequency Doppler system. Ph.D. thesis, University of Colorado, 242 pp.

Ecklund, W. L., D. A. Carter, and B. B. Balsley, 1988: A UHF wind profiler for the boundary layer: Brief description and initial results. *J. Atmos. Oceanic Technol.,* **5,** 432–441.

——, ——, ——, P. E. Currier, J. L. Green, B. L. Weber, and K. S. Gage, 1990: Field tests of a lower tropospheric wind profiler. *Radio Sci.,* **25,** 899–906.

Gage, K. S., and B. B. Balsley, 1978: Doppler radar probing of the clear atmosphere. *Bull. Amer. Meteor. Soc.,* **59,** 1074–1093.

——, J. L. Green, and T. E. VanZandt, 1980: Use of Doppler radar for the measurement of atmospheric turbulence parameters from the intensity of clear-air echoes. *Radio Sci.,* **15,** 407–416.

——, B. B. Balsley, W. L. Ecklund, D. A. Carter, and J. R. McAfee, 1991: Wind profiler–related research in the tropical Pacific. *J. Geophys. Res.,* **96,** 3209–3220.

Gossard, E. E., 1988: Measuring drop-size distributions in clouds with a clear-air-sensing Doppler radar. *J. Atmos. Oceanic Technol.,* **5,** 640–649.

——, 1990: Radar research on the atmospheric boundary layer. *Radar in Meteorology,* D. Atlas, Ed., Amer. Meteor. Soc., 477–527.

——, R. G. Strauch, and R. R. Rogers, 1990: Evolution of drop-size distribution in liquid precipitation observed by ground-based Doppler radar. *J. Atmos. Oceanic Technol.,* **7,** 815–828.

Gunn, R., and G. D. Kinzer, 1949: The terminal velocity of fall for water drops in stagnant air. *J. Meteor.,* **6,** 243–248.

Lavoie, R. L., 1967: Air motions over the windward coast of the island of Hawaii. *Tellus,* **19,** 354–358.

Law, D. C., 1991: Effects of precipitation, convection, and waves on NOAA network profilers. Preprints, *25th Intl. Conf. on Radar Meteorology,* Paris, Amer. Meteor. Soc., 43–46.

Neff, W., J. Jordan, J. Gaynor, D. Wolfe, W. Ecklund, D. Carter, and K. Gage, 1991: The use of 915 MHz wind profilers in complex terrain and regional air quality studies. Preprints, *7th Joint Conf. on Applications of Air Pollution Meteorology,* New Orleans, Amer. Meteor. Soc., J230–J233.

Probert-Jones, J. R., 1960: The analysis of Doppler radar echoes from precipitation. *Proc. 8th Weather Radar Conf.,* San Francisco, Amer. Meteor. Soc., 347–354.

Rasmussen, R. M., and P. K. Smolarkiewicz, 1993: On the dynamics of Hawaiian cloud bands. Part III: Local aspects. *J. Atmos. Sci.,* in press.

Rogers, R. R., and R. J. Pilié, 1962: Radar measurements of drop-size distribution. *J. Atmos. Sci.,* **19,** 503–508.

——, I. I. Zawadzki, and E. E. Gossard, 1991: Variation with altitude of the drop-size distribution in steady light rain. *Quart. J. Roy. Meteor. Soc.,* **117,** 1341–1369.

Strauch, R. G., D. A. Merritt, K. P. Moran, K. B. Earnshaw, and D. Van de Kamp, 1984: The Colorado wind-profiling network. *J. Atmos. Oceanic Technol.,* **1,** 37–49.

Tatarski, V. I., 1961: *Wave Propagation in a Turbulent Medium.* McGraw-Hill, 285 pp.

Wakasugi, K., A. Mizutani, M. Matsuo, S. Fukao, and S. Kato, 1986: A direct method for deriving drop-size distribution and vertical air velocities from VHF Doppler radar spectra. *J. Atmos. Oceanic Technol.,* **3,** 623–629.

——, ——, ——, ——, and ——, 1987: Further discussion on deriving drop-size distribution and vertical air velocities directly from VHF Doppler radar spectra. *J. Atmos. Oceanic Technol.,* **4,** 170–179.

White, A. B., and C. W. Fairall, 1991: Radar derived profiles of vertical velocity and turbulence dissipation rate in the convectively driven planetary boundary layer. Abstracts, *2nd Symp. on Lower Tropospheric Profiling,* Boulder, CO, National Center for Atmospheric Research, 155–156.

Wilson, J., D. Carter, W. Ecklund, K. Gage, M. Spowart, and H. Cole, 1991: First test of a ship-board wind profiler. Abstracts, *2nd Symp. on Lower Tropospheric Profiling,* Boulder, CO, National Center for Atmospheric Research, 157.